KeAi

CHINESE ROOTS
GLOBAL IMPACT

Contents lists available at ScienceDirect

# Petroleum Science

journal homepage: www.keaipublishing.com/en/journals/petroleum-science



# Original Paper

# Relative permeability estimation of oil—water two-phase flow in shale reservoir



Yu-Liang Su a, b, Ji-Long Xu a, b, Wen-Dong Wang a, b, \*, Han Wang a, b, Shi-Yuan Zhan a, b

- <sup>a</sup> Key Laboratory of Unconventional Oil & Gas Development, Ministry of Education, Qingdao 266580, Shandong, China
- b School of Petroleum Engineering, China University of Petroleum (East China), Qingdao 266580, Shandong, China

#### ARTICLE INFO

Article history:
Received 14 June 2021
Accepted 27 December 2021
Available online 30 December 2021
Handling Editor: Liang Xue
Edited by Yan-Hua Sun

Keywords: Shale Relative permeability Two-phase flow TOC Analytical model

## ABSTRACT

Oil—water two-phase flow is ubiquitous in shale strata due to the existence of connate water and the injection of fracturing fluid. In this work, we propose a relative permeability model based on a modified Hagen—Poiseuille (HP) equation and shale reconstruction algorithm. The proposed model can consider the nanoconfined effects (slip length and spatially varying viscosity), oil—water distribution, pore size distribution (PSD), total organic matter content (TOC), and micro-fracture. The results show that the increasing contact angles of organic matters (OM) and inorganic minerals (iOM) increase the relative permeability of both oil and water. As the viscosity ratio increases, the relative permeability of oil phase increases while that of water phase decreases, due to the different water—oil distribution. The effective permeability of both oil and water decreases with the increasing TOC. However, the relative permeability of water phase increases while that of oil phase decreases. The increasing number and decreasing deviation angle of micro-fracture increase the effective permeability of oil and water. However, micro-fracture has a minor effect on relative permeability. Our model can help understand oil—water two-phase flow in shale reservoirs and provide parameter characterization for reservoir numerical simulation.

© 2022 The Authors. Publishing services by Elsevier B.V. on behalf of KeAi Communications Co. Ltd. This is an open access article under the CC BY-NC-ND license (http://creativecommons.org/licenses/by-nc-nd/4.0/).

#### 1. Introduction

In recent years, shale oil has attracted tremendous attention to offset the declining production in conventional resources (Naraghi and Javadpour, 2015a; Cao et al., 2017). Horizontal drilling and multi-stage hydraulic fracturing are recognized as the most reliable techniques to extract shale oil (Tahmasebi et al., 2015; Wang et al., 2015b). In this process, the injection of drilling fluid, fracturing fluid, and the existence of initial water lead to widespread oil—water two-phase flow in shale strata. Therefore, understanding the oil—water two-phase flow behavior is significantly important for exploiting shale oil. Relative permeability is not only the cornerstone of production optimization, but also a bridge between microscale flow mechanism and macroscale numerical simulation. It has been proven to be a suitable tool to characterize the complicated multiphase flow behavior in porous media.

There are three approaches for determining the relative permeability (Zhang et al., 2017b; Wang et al., 2019): (1) experimental measurement, (2) numerical simulation, (3) analytical modeling. Experimental methods for measuring relative permeability can be divided into two types, that is steady state method and unsteady state method (Honarpour and Mahmood, 1988; Chen et al., 2016). However, the ultra-low permeability and multiscale structure of shale make the steady-state method extremely timeconsuming (Kianinejad et al., 2016). For the unsteady state method, the pressure drop and effluent fractional flow in the measurement process are seriously disturbed by capacity end effect (Wang et al., 2019). Therefore, it is quite challenging and even impossible to measure the relative permeability of unconventional reservoirs. The numerical simulation methods, mainly including pore-network model (Cui et al., 2019) and the Lattice Boltzmann method (Ba et al., 2016), are powerful tools to investigate the oil—water flow. However, these methods are also time-consuming and difficult to quantitatively characterize the effects of physical parameters, such as pore wall wettability (Wang et al., 2019). The analytical modeling methods can be further divided into types:

<sup>\*</sup> Corresponding author. School of Petroleum Engineering, China University of Petroleum (East China), Qingdao 266580, Shandong, China.

E-mail address: wwdong@upc.edu.cn (W.-D. Wang).

continuum and discrete. The continuum methods are based on the continuum scale representation of porous media and use fractal and other means to calculate the relative permeability. They are computationally fast and can quantify the effects of various physical parameters. However, the influence of micro-fractures and laminations in shale cannot be considered (Singh and Cai, 2019). By contrast, the discrete methods rely on shale reconstruction, which can characterize various geological controls of shale, such as pore size distribution (PSD), total organic matter content (TOC), fractures, etc. What's more, the idealized pore structure used in each discrete cell is convenient to describe the nanoconfined effects of fluid flow in nanopores, such as velocity slip and spatially varying viscosity.

Two major components exist in shale rocks: organic matter (OM) and inorganic minerals (iOM) (Naraghi et al., 2018). The pore sizes of the two components mainly range from a few nanometers to several hundred nanometers (Clarkson et al., 2013; Naraghi and Javadpour, 2015b; Rafatian and Capsan, 2015), while the aperture of microfractures in shale can reach several microns (Fig. 1). Due to the different nature of OM and iOM, the fluid flow mechanism is also quite different. The OM is mainly composed of kerogen, which is a typical hydrophobic component. When oil-water two-phase flow is laminar in OM nanopores, the water phase distributes in the center of the pores and is surrounded by the oil phase. Experiments and molecular dynamic (MD) simulations have proved that oil molecules have a large velocity slip on the wall of the organic pore, such as graphene and carbon nanotubes (CNTs) (Majumder et al., 2005; Wang et al., 2016). The slip length, defined as the distance extrapolated from the pore wall where the tangential velocity component disappears (Zhang et al., 2018), can reach hundreds of nanometers, much larger than the diameter of the pore. What's more, due to the strong oil-wall molecular interactions, an adsorbed region with a thickness of about four molecules will be formed near the wall, showing different density and viscosity characteristics from bulk oil (Wang et al., 2015a). Additionally, there is an interface region between the bulk oil and bulk water. In such regions, oil and water maintain distinct molecular speeds, resulting in a velocity jump, which is named liquid-liquid slip (Koplik and Banavar, 2006; Li et al., 2019). At the same time, both the viscosity and density of this region are smaller than those of bulk oil and bulk water (Zhan et al. 2020a, 2020b). When oil and water transport in the nanopores of iOM (such as quartz and clay, etc.) (Fang et al., 2019; Zhang et al., 2019a), there is also an adsorbed region, an interface region and two bulk phase regions, but the oil becomes a non-wetting phase and distributes in the pore center. The

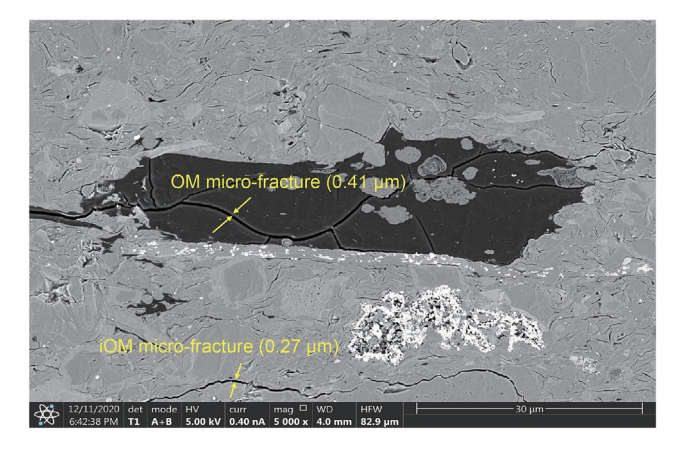
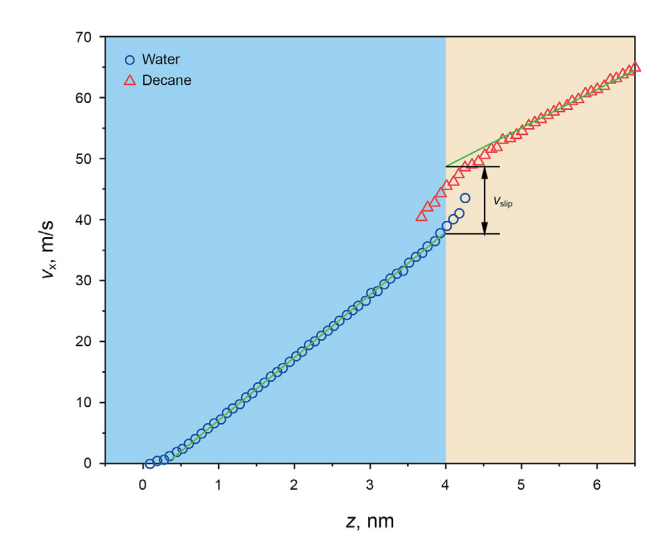


Fig. 1. SEM images of shale from Dagang Oilfield, China. The black parts represent OM, while others are iOM.

adsorbed region has two or three molecular layers of water showing high viscosity, which is named "multilayer sticking". What's more, the slip length of water on different walls is strongly dependent on the contact angle (Huang et al., 2008). In conclusion, velocity slip and spatially varying viscosity defy the traditional non-slip Hagen—Poiseuille (H—P) equation (Zhang et al., 2017a). It is important to consider the contribution of adsorbed, interface, and bulk regions respectively in the relative permeability calculation (Zhan et al., 2020a).

An extensive body of literature has discussed the theoretical calculation of fluid flow in nanopores. To calculate the water flow rate in CNTs, Mattia and Calabrò (2012) first divided the water into near-wall and bulk regions. The velocity in each region obeys the slip-modified H–P equation. Followed by, the model was extended to the oil flow in organic and inorganic nanopores to calculate apparent permeability (Cui et al., 2017; Zhang et al., 2017a; Sun et al., 2019). The differences between these models are the thickness, viscosity, and slip length of the near-wall region. In recent years, this method has been proven to be suitable for two-phase flow. Yiotis et al. (2007) calculated the relative permeability by only dividing the fluid into two regions: wetting bulk phase and non-wetting bulk phase. Cui et al. (2019) and Singh and Cai (2019) further considered the adsorbed region when calculated the relative permeability using pore network and discrete analytic model, respectively. To describe the velocity jump at the interface region, Navier slip condition (Koplik and Banavar, 2006; Zhang et al., 2017b; Fang et al., 2019) and apparent viscosity (Wang et al., 2019; Zhan et al. 2020a, 2020b) are usually used. The Navier slip condition can be expressed as  $v_{\text{slip}} = \alpha \cdot \tau$ , in which  $v_{\text{slip}}$  is the velocity difference between two immiscible fluids that are extrapolated from their bulk phases to the nominal interface (Fig. 2) (Fang et al., 2019);  $\tau$  and  $\alpha$  are the shear stress and Navier coefficient, respectively. The apparent viscosity method assumes that the velocity between each region is still continuous. Using MD simulations, Zhan et al. (2020b) deeply studied the liquid-liquid slip of oil (simplified as octane) and water in quartz nano-slit. They found that apparent interface viscosity is more effective to characterize the liquid-liquid slip because it does not change with driving force and pore size. By dividing the oil-water flow region into four regions: adsorbed water region, bulk water region, oil-water interface region



**Fig. 2.** Velocity profiles of water and decane in quartz (Fang et al., 2019).  $v_{\rm slip}$  is the velocity difference between decane phase and water phase at the interface. The interface is defined as the position where the density of decane is half of its bulk value.

(OWIR), and bulk oil region, and applying the slip modified H–P equation in each region, their model (P-model) is in excellent agreement with the results of MD simulations.

In this study, based on the P-model, the oil—water flow rates in circular nanopores and slit fractures of OM and iOM are derived respectively in Section 2.1. Then, in Section 2.2, a discrete spatial distribution (DSD) model of shale components (OM and iOM) is established by Quartet Structure Generation Set (QSGS) algorithm. What's more, the micro-fractures are also constructed in the DSD model by the discrete fracture method. By integrating the P-Model and DSD model, we finally get the relative permeability of the representative elementary volume (REV) scale in Section 2.3 and validate it in Section 2.4. Finally, in Section 3, the effect of wettability, viscosity ratio, TOC, and micro-fracture on relative permeability are discussed.

#### 2. Mathematical modeling

# 2.1.~ Oil—water two-phase flow in circular nanopore and slit micro-fracture

In this section, we first build oil—water two-phase flow models in pores and microfractures and derive the analytical expressions of volume flux, respectively. Then we discuss the value of the parameters in the expressions based on the results of experiments, MD simulations, and theoretical analysis.

#### 2.1.1. Two-phase flow theoretical model

The oil—water distribution in OM/iOM pores and microfractures is shown in Fig. 3. Based on the results of MD simulations (Li et al., 2019; Zhan et al., 2020a) and the P-model of (Zhan et al., 2020b). The flow spaces in pores and micro-fractures are all divided into four regions. In the OM pore (Fig. 3(a)), the velocity in different regions can be expressed as follows.

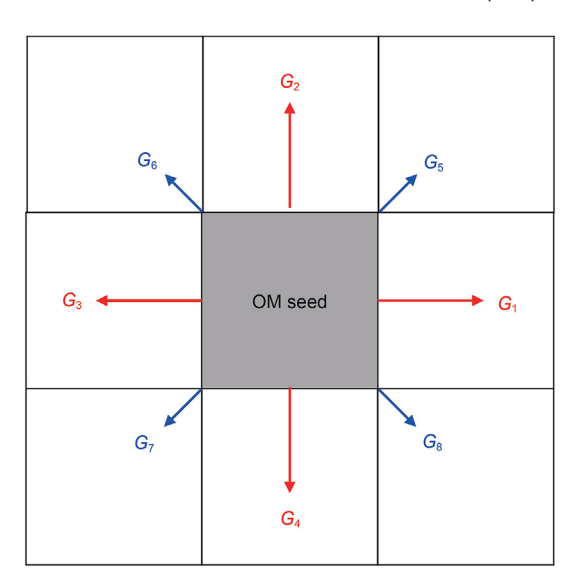


**Fig. 4.** Eight growth directions of seed. The length of arrows indicates the relative value of the growth probability. An isotropic structure of OM particle should set  $G_{1.4}$ :  $G_{5.8} = 4$  (Wang et al., 2007).

Bulk water region:

$$v_{\text{wb}}^{\text{p,OM}}(r) = \frac{\Delta p}{L} \frac{R^2 - r^2}{4\mu_{\text{wb}}} + c_1^{\text{p,OM}}, r \in [0, h_{\text{w}}]$$
(1)

owir

$$v_{\text{o-w}}^{\text{p,om}}(r) = \frac{\Delta p}{L} \frac{R^2 - r^2}{4\mu_{\text{o-w}}} + c_2^{\text{p,om}}, r \in [h_{\text{w}}, h_{\text{w}} + \delta_{\text{o-w}}]$$
 (2)

Bulk oil region:

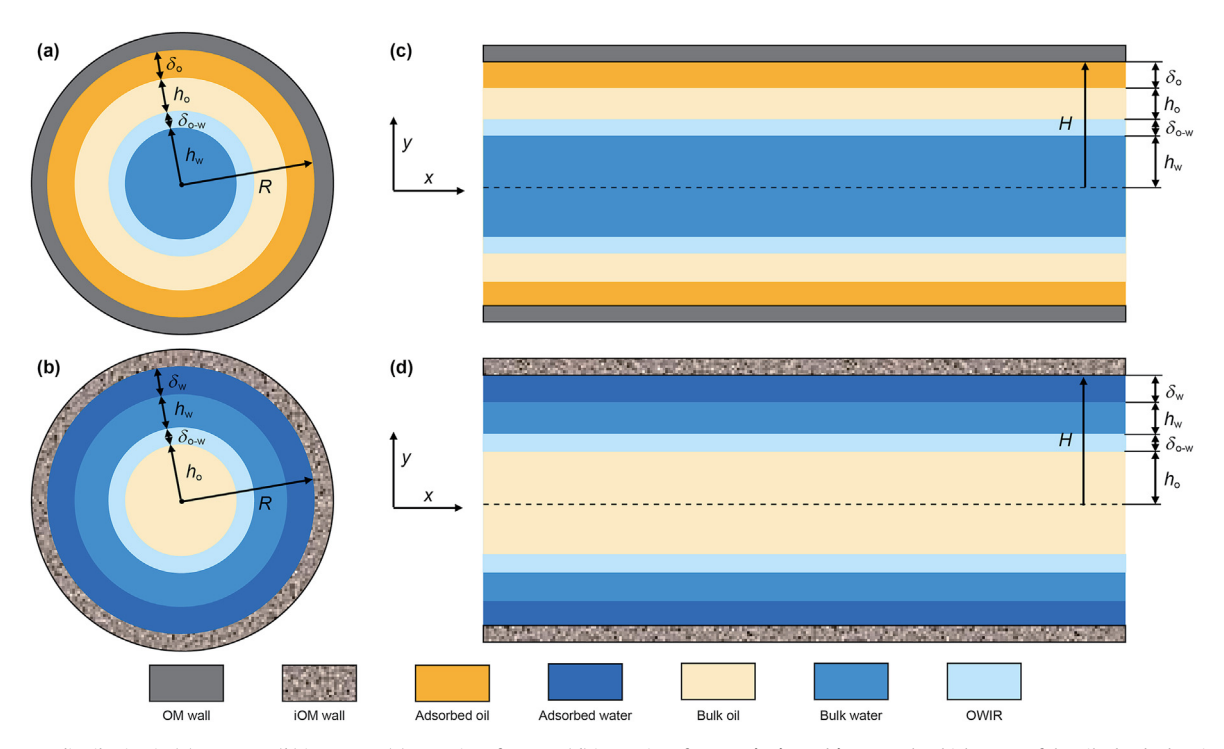


**Fig. 3.** Oil—water distribution in (**a**) OM pore; (**b**) iOM pore; (**c**) OM micro-fracture; (**d**) iOM micro-fracture.  $\delta_0$ ,  $\delta_w$  and  $\delta_{0-w}$  are the thicknesses of the oil adsorbed region, adsorbed water region, and the oil—water interface region respectively;  $h_0$  and  $h_w$  are the thicknesses of the bulk oil region and bulk water region respectively; R is the radius of circular pore; R is the half aperture of micro-fracture.

$$v_{\text{ob}}^{\text{p,OM}}(r) = \frac{\Delta p}{L} \frac{R^2 - r^2}{4\mu_{\text{ob}}} + c_3^{\text{p,OM}}, r \in [h_{\text{w}} + \delta_{\text{o-w}}, R - \delta_{\text{o}}]$$
(3)

Adsorbed oil region:

$$v_{\text{on}}^{\text{p,OM}}(r) = \frac{\Delta p}{L} \frac{R^2 - r^2}{4\mu_{\text{on}}} + c_4^{\text{p,OM}}, r \in [R - \delta_0, R]$$
 (4)

where  $v_{\mathrm{wb}}^{\mathrm{p,OM}}$ ,  $v_{\mathrm{o-w}}^{\mathrm{p,OM}}$ ,  $v_{\mathrm{ob}}^{\mathrm{p,OM}}$ ,  $v_{\mathrm{ob}}^{\mathrm{p,OM}}$  and  $\mu_{\mathrm{wb}}$ ,  $\mu_{\mathrm{o-w}}$ ,  $\mu_{\mathrm{ob}}$ ,  $\mu_{\mathrm{on}}$  are the velocity and viscosity of bulk water, OWIR, bulk oil, and adsorbed oil in OM pore respectively;  $c_1^{\mathrm{p,OM}}$ ,  $c_2^{\mathrm{p,OM}}$ ,  $c_3^{\mathrm{p,OM}}$  and  $c_4^{\mathrm{p,OM}}$  are the corrected coefficients considering slip length and spatially varying viscosity in OM pore;  $\frac{\Delta p}{L}$  is the externally applied pressure gradient; r is the length from the pore center.

If the apparent viscosity method is used in the OWIR, the velocity between different regions is continuous, and the boundary conditions should satisfy:

$$Q_{\text{wb}}^{\text{p,OM}} = \int_{0}^{h_{\text{w}}} v_{\text{wb}}^{\text{p,OM}} 2\pi r dr = \int_{0}^{h_{\text{w}}} \left( \frac{\Delta p}{L} \frac{R^2 - r^2}{4\mu_{\text{wb}}} + c_1^{\text{p,OM}} \right)$$

$$2\pi r dr = \frac{\Delta p}{L} \frac{\pi}{4\mu_{\text{wb}}} \left( R^2 h_{\text{w}}^2 - \frac{h_{\text{w}}^4}{2} \right) + \pi c_1^{\text{p,OM}} h_{\text{w}}^2$$
(10)

$$\begin{split} Q_{\text{0-W}}^{\text{p,OM}} &= \int\limits_{h_{\text{w}}}^{h_{\text{w}} + \delta_{\text{0-w}}} v_{\text{0-W}}^{\text{p,OM}} 2\pi r dr = \int\limits_{h_{\text{w}}}^{h_{\text{w}} + \delta_{\text{0-w}}} \left( \frac{\Delta p}{L} \frac{R^2 - r^2}{4\mu_{\text{0-W}}} + c_2^{\text{p,OM}} \right) \\ 2\pi r dr &= \frac{\Delta p}{L} \frac{\pi}{4\mu_{\text{0-W}}} \left[ R^2 (h_{\text{w}} + \delta_{\text{0-w}})^2 - R^2 h_{\text{w}}^2 - \frac{(h_{\text{w}} + \delta_{\text{0-w}})^4}{2} + \frac{h_{\text{w}}^4}{2} \right] \\ &+ \pi c_2^{\text{p,OM}} \left[ (h_{\text{w}} + \delta_{\text{0-w}})^2 - h_{\text{w}}^2 \right] \end{split}$$

$$(11)$$

$$Q_{ob}^{p,OM} = \int\limits_{h_{w}+\delta_{o-w}}^{R-\delta_{o}} \nu_{ob}^{p,OM} 2\pi r dr = \int\limits_{h_{w}+\delta_{o-w}}^{R-\delta_{o}} \left( \frac{\Delta p}{L} \frac{R^{2}-r^{2}}{4\mu_{ob}} + c_{3}^{p,OM} \right) 2\pi r dr = \frac{\Delta p}{L} \frac{\pi}{4\mu_{ob}} \left[ R^{2}(R-\delta_{o})^{2} - R^{2}(h_{w}+\delta_{o-w})^{2} - \frac{(R-\delta_{o})^{4}}{2} + \frac{(h_{w}+\delta_{o-w})^{4}}{2} \right] \\ + \pi c_{3}^{p,OM} \left[ (R-\delta_{o})^{2} - (h_{w}+\delta_{o-w})^{2} \right]$$
 (12)

$$Q_{on}^{p,OM} = \int_{R-\delta_o}^{R} \nu_{on}^{p,OM} 2\pi r dr = \int_{R-\delta_o}^{R} \left( \frac{\Delta p}{L} \frac{R^2 - r^2}{4\mu_{on}} + c_4^{p,OM} \right) 2\pi r dr = \frac{\Delta p}{L} \frac{\pi}{4\mu_{on}} \left[ R^4 - R^2 (R - \delta_o)^2 - \frac{R^4}{2} + \frac{(R - \delta_o)^4}{2} \right] + \pi c_4^{p,OM} \left[ R^2 - (R - \delta_o)^2 \right]$$

$$\tag{13}$$

$$\left. \frac{\partial v_{wb}^{p,OM}}{\partial r} \right|_{r=0} = 0 \tag{5}$$

$$v_{\text{wb}}^{\text{p,OM}}\Big|_{r=h_{\text{w}}} = v_{\text{o-w}}^{\text{p,OM}}\Big|_{r=h_{\text{w}}} \tag{6}$$

$$v_{\text{ob}}^{\text{p,OM}}\Big|_{r=h_{\text{w}}+\delta_{\text{o-w}}} = v_{\text{o-w}}^{\text{p,OM}}\Big|_{r=h_{\text{w}}+\delta_{\text{o-w}}}$$

$$\tag{7}$$

$$v_{\text{on}}^{\text{p,OM}}\Big|_{r=R-\delta_0} = v_{\text{ob}}^{\text{p,OM}}\Big|_{r=R-\delta_0}$$
(8)

$$-l_{os} \frac{\partial v_{on}^{p,OM}}{\partial r}\bigg|_{r=R} = v_{on}^{p,OM}\bigg|_{r=R}$$
(9)

where  $l_{\rm os}$  is the slip length of oil. Combing Eqs. (1)–(9), the corrected coefficients are calculated and presented in Supporting Information. Then the volume fluxes in each region can be obtained by:

where  $Q_{wb}^{p,OM}$ ,  $Q_{o-w}^{p,OM}$ ,  $Q_{ob}^{p,OM}$  and  $Q_{on}^{p,OM}$  are the volume fluxes of bulk water, OWIF, bulk oil and adsorbed oil in OM pore respectively. The corresponding total volume fluxes of oil and water can be expressed as:

$$Q_{o}^{p,OM} = Q_{ob}^{p,OM} + Q_{on}^{p,OM} + (1 - f_{w})Q_{o-w}^{p,OM}$$
(14)

$$Q_{W}^{p,OM} = Q_{Wb}^{p,OM} + f_{W}Q_{o-W}^{p,OM}$$
 (15)

where  $f_W$  is the proportion of water volume fluxes in the OWIF volume fluxes.

According to the thickness of each region, the water saturation in OM pore can be expressed as:

$$s_{w}^{p,OM} = \frac{\pi V_{w} (h_{w} + \delta_{o-w})^{2} - \pi V_{w} h_{w}^{2} + \pi h_{w}^{2}}{\pi R^{2}}$$

$$= \frac{V_{w} (h_{w} + \delta_{o-w})^{2} + h_{w}^{2} (1 - V_{w})}{R^{2}}$$
(16)

where  $V_{\rm W}$  is the volume proportion of water in the OWIF, which equals 0.5 because the oil and water occupy the same volume in OWIF (Zhan et al., 2020b). Based on similar methods, the volume fluxes and water saturation in iOM pores and microfractures of OM and iOM can be obtained, and the details are summarized in Supporting Information.

#### 2.1.2. Parameter value of the two-phase flow theoretical model

The value of three types of parameters should be discussed before using the theoretical model: (1) slip length of oil and water in adsorbed region, (2) thickness of each flow region, (3) viscosity of each flow region.

In MD simulations, researchers usually use two models to characterize OM of shale: graphene (Bui and Yucel Akkutlu, 2017; Nan et al., 2020) and kerogen molecular model (Collell et al., 2015; Perez and Devegowda, 2020; Yang et al., 2020). Wang et al. (2016) studied the octane flow in graphene slit and they found that about 2-4 adsorption layers of oil molecules were formed, depending on the slit size. What's more, they studied the slip length at different slit sizes, driving forces and temperatures. The results show that the slip length in the slit of several nanometers can be more than 100 nm, so that the velocity profile deviated from parabolic to plug. The large slip length can be attributed to the ultra-smoothness of graphene surface (Joseph and Aluru, 2008), which is unrealistic in shale. Although some researchers have studied the oil flow in pores composed of real kerogen molecules (Falk et al., 2015; Liu et al., 2020), they have not given a quantitative expression for the slip length. Recently, Wu et al. (2019) derived the slip length of *n*-alkanes transporting in nanopores based on the different mobility of the first-layer n-alkanes and bulk n-alkanes. The results showed good agreement with MD and experiments, and can be expressed as:

$$l_{\rm os} = \delta \left( \frac{\tau_{\infty}}{\tau_{\rm b}} e^{\frac{\pi (0.1265(n-1)+0.46)^2 \sigma_{\rm l} (1-\cos\theta_{\rm o})}{6KT}} - 1 \right)$$
 (17)

where  $\delta$  is the average distance between n-alkane molecules in adjacent layers, which is about 0.5 nm;  $\frac{\tau_\infty}{\tau_b}$  is the ratio of the natural relaxation time of bulk molecules to that of the first adsorbed molecules on the wall, which is about 0.45 for octane in OM pores (Gupta et al., 1994); n is the carbon numbers of n-alkanes;  $\sigma_1$  is the surface tension of n-alkanes in vacuum, which can be obtained from National Institute of Standards and Technology (NIST);  $\theta_0$  is the contact angle of oil; K and T are Boltzmann constant and temperature, respectively.

In addition, Wu et al. (2019) gave the ratio of the viscosity of the adsorbed oil region ( $\delta_0=1$  nm) to the bulk oil region as:

$$\frac{\mu_{\rm on}}{\mu_{\rm ob}} = \frac{\tau_i}{\tau_{\infty}} \tag{18}$$

where  $\tau_i$  is the average natural relaxation time of the n-alkanes in the adsorbed region, which can be expressed as:

$$\tau_i = 0.5(\tau_{\infty} + \tau_{\rm b}) \tag{19}$$

For the nanoconfined flow of water, the slip length can also be expressed by the contact angle (Wu et al., 2017):

$$l_{\rm ws} = \frac{0.41}{(1 + \cos\theta_{\rm w})^2} \tag{20}$$

where  $l_{ws}$  and  $\theta_{w}$  are the slip length and contact angle of water, respectively. What's more, the ratio of the viscosity of the adsorbed water region ( $\delta_{w}=0.7~\text{nm}$ ) to the bulk water region can be expressed as:

$$\frac{\mu_{\rm wn}}{\mu_{\rm wb}} = -0.018\theta_{\rm w} + 3.25\tag{21}$$

Based on MD simulations, Zhan et al. (2020b) found that the thickness and viscosity of OWIR were about  $\delta_{0-w}=0.35$  nm and  $\mu_{0-w}=0.22$  mPa·s =  $0.29(\mu_{0b}+\mu_{wb})$  respectively under a typical reservoir condition (323 K and 20 MPa), and do not change with driving force and pore size. However, the flux contribution of water and oil depends on the pore size. In iOM pores the water molecules transport slower than oil (Fig. 2), so  $f_w$  should smaller than 0.5 (larger than 0.5 in OM pores). However, the  $f_w$  gradually equals 0.5 with the increase in water film (i.e.  $\delta_w+h_w$ ) in quartz nano slits (Zhan et al., 2020b). Because the minimum of water film thickness in our model is equal to 0.7 nm, we set  $f_w=0.5$ .

Now only the thickness of the bulk oil region or the bulk water region has not been determined. Taking oil—water two-phase flow in OM pores as an example, when there are too few water molecules to cover the wall, water cannot form a continuous phase in the pore (Li et al., 2019), so the theoretical model shown in Fig. 3(a) and (c) is invalid. Similarly, oil molecules cannot form a continuous phase if the number of oil molecules is not enough. Therefore, to use the theoretical model reasonably, we assume that the thickness range of the bulk oil region is  $(0, R - \delta_{0-W} - \delta_0)$ , and the adsorbed region and OWIR always exist. Therefore, according to Eq. (16), the range of  $s_W$  of an OM pore can be expressed as Eq. (22), and the range of  $s_W$  in iOM pore and micro-fractures are listed in Supporting Information.

$$\left( \frac{V_{w}(\delta_{o-w})^{2}}{R^{2}}, \frac{V_{w}(R-\delta_{o})^{2} + (R-\delta_{o-w}-\delta_{o})^{2}(1-V_{w})}{R^{2}} \right) \tag{22}$$

# 2.2. The discrete spatial distribution model of shale components and micro-fractures

QSGS (Wang et al., 2007) has been widely used to mimic the formation of porous media because it can characterize the volume fraction, average particle size, and particle shape of each phase. In this study, we employ QSGS to reconstruct the shale, which begins with a grid  $L_X \times L_y$  ( $L_X$  and  $L_Y$  are the grid length along the X and Y directions) merely filled with iOM. Parameters used are listed in Table 1 and the steps are as follows:

(1) **Seeding:** Randomly select several cells of grid as OM seeds based on a distribution probability  $p_{\rm d}$ .  $p_{\rm d}$  is related to the TOC and average particle size ( $r_{\rm OM}$ ) of OM, which can be set as:

$$p_{\rm d} = \frac{L_{\rm x}L_{\rm y} {\rm TOC}}{Kr_{\rm OM}^2 N} \tag{23}$$

where K is the shape factor, and  $K = \pi$  when the particle is circular; N is the number of cells in the grid.

- (2) **Growth:** Grow the seeds to the neighboring cells in eight directions based on the growth probability  $G_i$  (Fig. 4).
- (3) Repeating: Repeat step (2) until the fraction of OM in the grid equals TOC.

To facilitate the investigation of the effect of fracture properties on relative permeability in Section 3.5. In this study, without losing generality, we set the length, aperture, and orientation of different micro-fractures to the same value (Table 1). For a specific shale, these properties can be extracted from SEM images (Feng et al.,

**Table 1**Basic parameters used in our model.

Parameters	Symbol	Value
Grid size	$L_{x} \times L_{y}$	150 μm × 150 μm
Cell numbers	N	$150 \times 150$
Total organic carbon content	TOC	0.2
The average particle size of OM	$r_{ m OM}$	16 μm
Directional growth probability	$G_i$	$G_{1:4}:G_{5:8}=4$
Micro-fracture orientation	β	30°
Micro-fracture length	$l_{\mathrm{f}}$	30 μm
Micro-fracture number	$n_{ m f}$	3
Micro-fracture aperture	Н	0.15 μm
Pore size distribution	PSD	OM: $\mu = 3.4012$ , $\sigma = 0.3$ iOM: $\mu = 2.326$ , $\sigma = 0.3$
Porosity	$\varphi$	0.1
Tortuosity	au	1
Contact angle	$\theta_{ m o}$ or $\theta_{ m w}$	$ heta_{ m W} = 60^{\circ};   heta_{ m o} = 60^{\circ}$
Slip length of oil	$l_{os}$	$0.225 \mathrm{e}^{4(1-\cos heta_\mathrm{o})} - 0.5$
Slip length of water	$l_{ m ws}$	$l_{ws} = \frac{0.41}{(1 + \cos\theta_{w})^2}$
Thickness of adsorbed region	$\delta_{ m o}$ or $\delta_{ m w}$	$\delta_0 = 1 \text{ nm}; \ \delta_W = 0.7 \text{ nm}$
Thickness of OWIR	$\delta_{ m o-w}$	0.35 nm
Viscosity of bulk water	$\mu_{wb}$	0.8 mPa s
Oil-water viscosity ratio	M	1
Viscosity of adsorbed phase	$\mu_{\rm on}$ or $\mu_{\rm wn}$	$\mu_{\rm on} = 1.61 \mu_{\rm ob}$
-		$\mu_{\rm wn} = (-0.018\theta_{\rm w} + 3.25)\mu_{\rm wb}$
Viscosity of OWIR	$\mu_{o-w}$	$0.29(\mu_{\rm ob} + \mu_{\rm wb})$
Water fluxes proportion in OWIF	fw	0.5

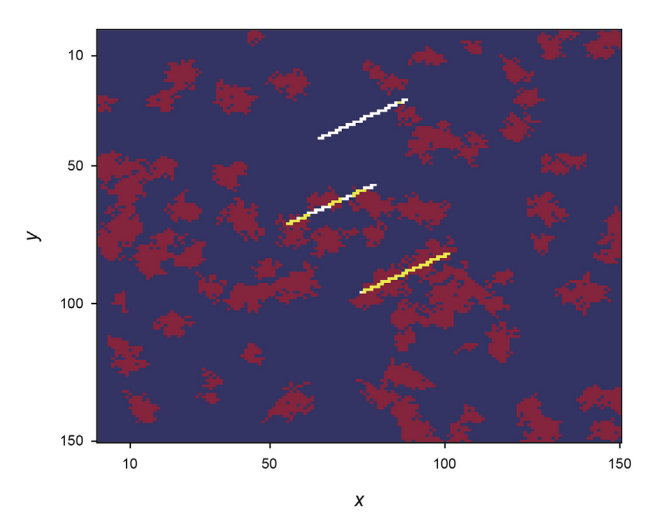


**Fig. 5.** DSD model of shale components and micro-fractures. The dark red, dark blue, bright yellow, and white parts represent OM, iOM, micro-fractures in OM, and micro-fractures in iOM respectively.

2019) or calculated by the probability distribution function (PDF) (Neuman, 2008; Sun et al., 2016). The steps of generating microfractures in the grid are similar to the QSGS algorithm.

- 1) Randomly select a cell as a fracture seed, and grow it along the given direction  $(\beta)$  until the length in the grid is equal to the given length  $(l_f)$ .
- 2) Repeat step (1) until the number of micro-fracture in the grid equals the given number  $(n_{\rm f})$ .

Fig. 5 shows the DSD model generated based on the parameters listed in Table 1.

# 2.3. Relative permeability of REV scale

The range of pore sizes within the OM is usually an order of

magnitude smaller than that of iOM, causing a bimodal PSD (Naraghi and Javadpour, 2015a). Therefore, the logarithmic normal distribution with different logarithmic means and logarithmic standard deviations can be used to characterize the pore size in OM and iOM, respectively, which can be expressed as (Zhang et al., 2019b):

$$f(R) = \frac{1}{R\sqrt{2\pi}\sigma} \exp\left[-\frac{1}{2} \left(\frac{\ln R - \mu}{\sigma}\right)^2\right]$$
 (24)

where  $\sigma$  and  $\mu$  are the logarithmic standard deviation and logarithmic mean, respectively.

The cells of DSD model can be divided into four types: OM pore cell, iOM pore cell, OM micro-fracture cell, and iOM micro-fracture cell. To characterize the PSD (Eq. (24)) of shale, the Monte Carlo sampling method is used to assign a pore size into each cell. Then, based on the two-phase flow theoretical model (Section 2.1) and capillary bundle model, we can calculate the effective permeability of oil and water in each cell. Taking an OM pore cell as an example, the total volume fluxes of oil and water in a cell can be expressed

$$Q_{o-t}^{p,OM} = N_c Q_o^{p,OM}$$
 (25)

$$Q_{W-f}^{p,OM} = N_c Q_W^{p,OM}$$
 (26)

where  $Q_{o-t}^{p, OM}$  and  $Q_{w-t}^{p, OM}$  are the total volume fluxes of oil and water in OM cell, respectively;  $N_c$  is the number of capillaries in the cell. According to Darcy's law, the volumetric fluxes can also be given by:

$$Q_{\rm o-t}^{\rm p,OM} = \frac{k_{\rm o}^{\rm p,OM} A}{\mu_{\rm ob}} \frac{\Delta p}{L} \tag{27}$$

$$Q_{W-t}^{p,OM} = \frac{k_W^{p,OM} A}{\mu_{wh}} \frac{\Delta p}{L}$$
 (28)

where  $k_0^{\mathrm{p,OM}}$  and  $k_\mathrm{w}^{\mathrm{p,OM}}$  are the effective permeability of oil and water; A is the cross-sectional area of the cell. Combing Eq. (25) to Eq. (28) and consider the tortuosity,  $k_0^{\mathrm{p,OM}}$  and  $k_\mathrm{w}^{\mathrm{p,OM}}$  can be expressed as:

$$k_o^{p,OM} = \frac{\phi Q_o^{p,OM} \mu_{ob}}{\tau \pi R^2} \frac{L}{\Delta p}$$
 (29)

$$k_{\rm w}^{\rm p,OM} = \frac{\phi Q_{\rm w}^{\rm p,OM} \mu_{\rm wb}}{\tau \pi R^2} \frac{L}{\Delta p} \tag{30}$$

where  $\tau$  is the tortuosity;  $\phi$  is the porosity, which can be written as:

$$\phi = \frac{N_{\rm c}\pi R^2}{A} \tag{31}$$

Similarly, the intrinsic permeability of a pore cell can be expressed as:

$$k_{\rm in} = \frac{\phi R^2}{8\tau} \tag{32}$$

Intrinsic permeability and effective permeability of oil and water in other types of cells are summarized in Supporting Information. After determining the effective and intrinsic permeability in each cell, the single-phase upscaling module in MATLAB Reservoir Simulation Toolbox (MRST) is used to upscale them respectively (Lie, 2019). Then the relative permeability of the REV scale can be expressed as:

$$k_{\text{ro-REV}} = \frac{k_{\text{o-REV}}}{k_{\text{in-REV}}} \tag{33}$$

$$k_{\text{rw-REV}} = \frac{k_{\text{w-REV}}}{k_{\text{in-REV}}} \tag{34}$$

where  $k_{\rm ro-REV}$  and  $k_{\rm rw-REV}$  are the relative permeability of oil and water in the REV scale, respectively;  $k_{\rm o-REV}$ ,  $k_{\rm w-REV}$  are the effective permeability of oil and water in the REV scale, respectively;  $k_{\rm in-REV}$  is the intrinsic permeability in the REV scale.

It should also be noted that according to Eq. (22), the range of water saturation is different because of the different pore sizes in each cell. In the following sections, when we calculate the relative permeability, we assume that each cell has the same water saturation, but if a given saturation is less than the lower limit of saturation in the cell, then the saturation is set as the lower saturation limit, and vice versa.

**Table 2**Basic parameters used in the model of Wang et al. (2019).

Parameters	Symbol	Value
Pore size distribution	PSD	iOM: $\mu = 2.327$ , $\sigma = 0.158$
Tortuosity	au	1
Contact angle	$\theta_{w}$	$ heta_{ m W}=30^\circ$
Slip length of water	$l_{ m ws}$	$l_{\rm ws} = \frac{6}{(1 + \cos\theta_{\rm w})^2}$
Thickness of adsorbed region	$\delta_{ m w}$	0.7 nm
Thickness of OWIR	$\delta_{ m o-w}$	0.35 nm
Viscosity of bulk water	$\mu_{\mathrm{wb}}$	0.8 mPa s
Oil-water viscosity ratio	M	0.3
Viscosity of adsorbed phase	$\mu_{ m wn}$	$(-0.018\theta_{\rm W} + 3.25)\mu_{\rm Wb}$
Viscosity of OWIR	$\mu_{o-w}$	$0.5(\mu_{\rm ob} + \mu_{\rm wb})$
Water fluxes proportion in OWIF	$f_{W}$	0.5

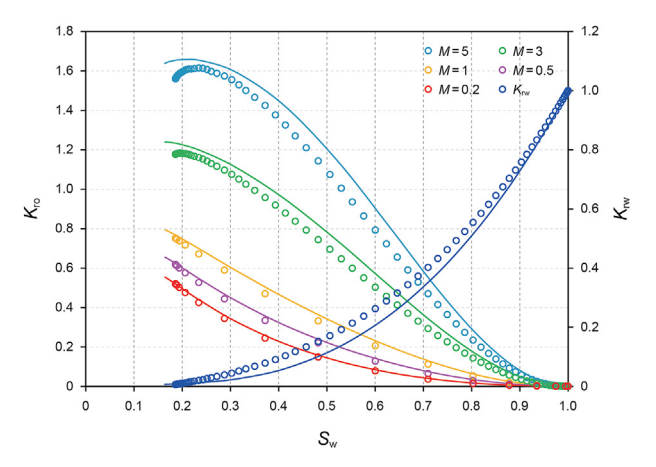


**Fig. 6.** Relative permeability of oil and water obtained by theoretical models ( $\theta_{\rm w}=30^\circ$ ,  $\mu_{\rm wb}=0.8$  mPa s). M is the ratio of bulk oil viscosity to bulk water viscosity. Only one set of water relative permeability curves is shown since it is independent of M. The solid lines are the results of our model, while the circles are calculated by Wang's model.

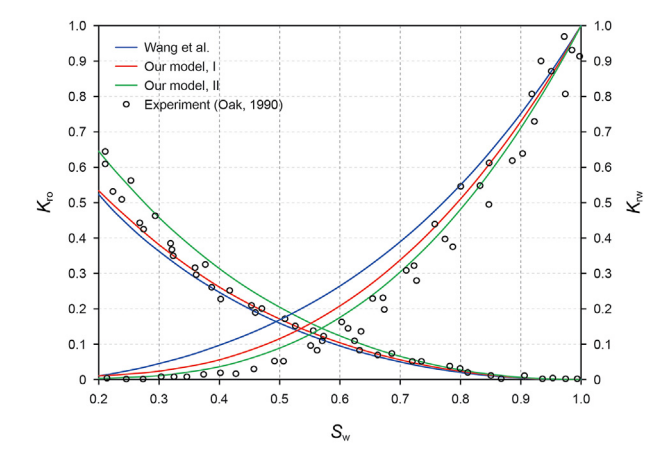
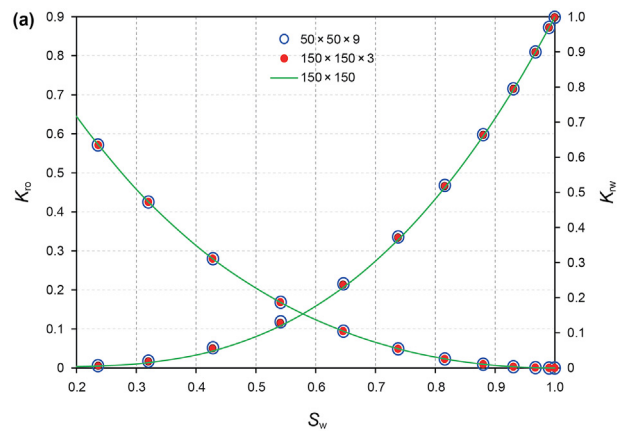


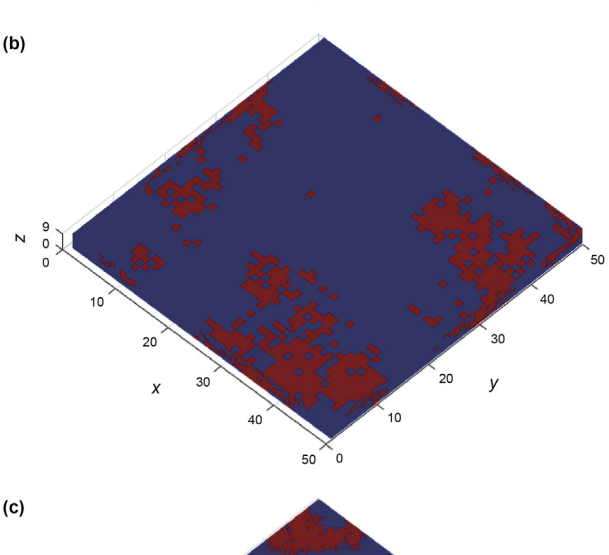
**Fig. 7.** Relative permeability of oil and water obtained by theoretical models and experiment ( $\theta_{\rm w}=30^{\circ}$ ,  $\mu_{\rm wb}=0.8$  mPa s, M=0.3). The blue and red solid lines are based on the parameters of Table 2, while the green solid lines are based on Table 1.

# 2.4. Model validation

Wang et al. (2019) constructed a relative permeability theoretical model of oil—water two-phase flow in iOM based on continuum method. However, OM pores and micro-fractures are not considered. Therefore, we simplify our model by setting TOC = 0 and  $n_f = 0$  for validation. The parameters used are listed in Table 2. It can be seen from the Fig. 6 that, compared with the results of Wang et al. (2019), our model slightly underestimates the relative permeability of water, while overestimates the relative permeability of oil. To further validate our model, we compared the results of our and Wang's models with the experimental data (Oak, 1990). As shown in Fig. 7, with the same parameters of Wang et al., our model are in better agreement with the experiment. What's more, if the parameters in Table 1 are used, the fitting accuracy will be higher. Therefore, the evaluation of relative permeability by our model is reliable.

The difference between the blue and red solid lines in Fig. 7 may be due to the way of upscaling relative permeability to the REV scale. The upscaling method used in Wang et al. (2019) is one-dimensional (1D), which only considers the permeability difference perpendicular to the fluid flow direction. However, the grid constructed in Section 2.2 is 2D, which the permeability difference parallel to the fluid flow direction can also be considered. We further construct two





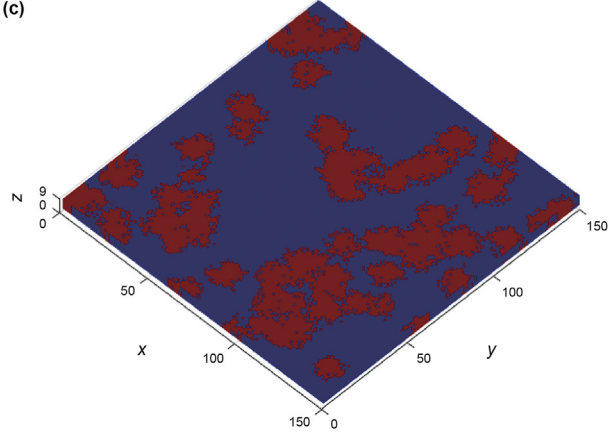


**Fig. 8.** (a) Relative permeability of oil and water obtained by 2D model and 3D models; (b) Grid with  $50 \times 50 \times 9$  cells; (c) Grid with  $150 \times 150 \times 3$  cells. The dark red parts in (b) and (c) represent OM, while others represent iOM. The TOC = 0.2 in (b) and (c), while TOC = 0 in (a).

3D grids to compare the results between them and the cell number are  $50 \times 50 \times 9$  (Fig. 8(b)) and  $150 \times 150 \times 3$  (Fig. 8(c)), respectively. As shown in Fig. 8(a), the difference in calculation results can be ignored completely. Therefore, the 2D model is more suitable due to its low computational cost.

#### 3. Results and discussion

In this section, firstly, the influence of nanoconfined effects (slip length and spatially varying viscosity) (Wu et al., 2017) on water-oil

two-phase flow in a single nanopore are elaborated. Then, we study the effects of wettability, viscosity ratio, TOC as well as microfracture on relative permeability. All the used parameters are listed in Table 1, unless otherwise specified.

# 3.1. Nanoconfined effects in single nanopore

Given the similar expression of fluid flux in pores and fractures, we only take pores as an example to analyze the influence of nanoconfined effects based on the enhancement factor:

$$\varepsilon = \frac{Q_{ti}}{Q_{ti-NO}} \tag{35}$$

where  $\varepsilon$  is the enhancement factor;  $Q_{ti}$  and  $Q_{ti-NO}$  are the fluid flux considering and ignoring nanoconfined effects, respectively; i = o, w represent the oil and water phase, respectively.

As shown in Fig. 9, both the slip length and OWIR apparent viscosity can strengthen the fluid flux, while the viscosity of adsorbed regions weakens the fluid flux. In OM nanopores, the effects of slip length and OWIR apparent viscosity are larger than the adsorbed oil viscosity, resulting  $\varepsilon > 1$  (Red lines in Fig. 9(a)). However, in iOM nanopores, the great adsorbed water viscosity strongly decreases the fluid flux, resulting  $\varepsilon$  < 1 (Red lines in Fig. 9(b)). The relative permeability curves shown in Fig. 10 indicates that shale is more hydrophilic in this case. As shown in the figure, the water saturation at the point of equal relative permeability is greater than 0.5. Two reasons can account for this. Firstly, the  $\varepsilon$  of oil phase is all larger than that of water phase. Secondly, although the water content (defined as the ratio of water flux to total fluid flux) of OM pores is greater than 0.5, the TOC is only 0.2, which limits the contribution of organic pores to relative permeability. In Section 3.4 we further discuss the effect of TOC on relative permeability.

Fig. 10 also shows the relative permeability curves with different PSD of iOM (OM results are similar). It can be reasonably inferred from Fig. 9 (b) that the increase of average pore size will reduce the relative permeability of oil phase and increase that of water phase. This is because the enhancement factor of water phase in a single nanopore increases faster with the increase of pore size.

## 3.2. Effects of wettability

The slip length and viscosity of the adsorbed regions are closely related to the contact angle. Therefore, it is attractive to investigate the influence of contact angle. In general, the OM is oil-wet while iOM is water-wet, so we calculated the relative permeability when contact angles are equal to 30°, 60°, and 90°, respectively. The increase in contact angle leads to the larger slip length and the smaller viscosity in the adsorbed regions, thus leading to the increase in effective permeability, while the intrinsic permeability of shale has nothing independent of contact angle. Therefore, with the increase in contact angle, both the relative permeability and effective permeability of oil phase and water phase increase as shown in Fig. 11.

## 3.3. Effects of viscosity ratio

The viscosity of shale oil varies greatly between different shale reservoirs and even within the same reservoir. Therefore, we study how the relative permeability changes with the oil—water viscosity ratio. As shown in Fig. 12, the relative permeability of oil phase increases with the increase in viscosity ratio and even can be larger than 1 when the ratio equals 2. This phenomenon is consistent with the conclusions of Wang et al. (2019) and Yiotis et al. (2007) and can

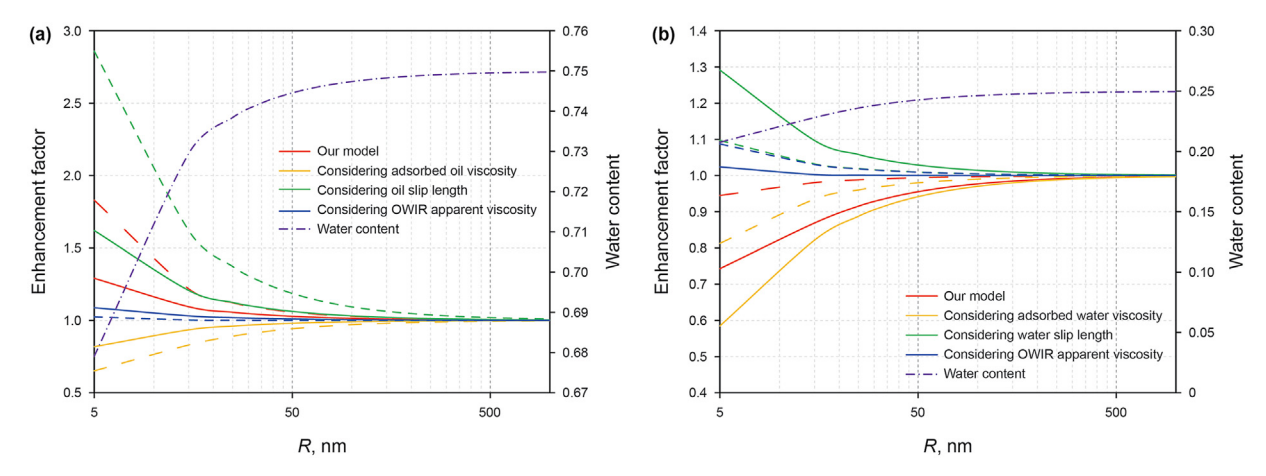


**Fig. 9.** Enhancement factor and water content considering different nanoconfined effects in OM ( $\bf a$ ) and iOM ( $\bf b$ ) nanopores ( $S_{\rm w}=0.5$ ). For enhancement factor curves, the solid lines represent water phase, while the dashed lines represent oil phase.

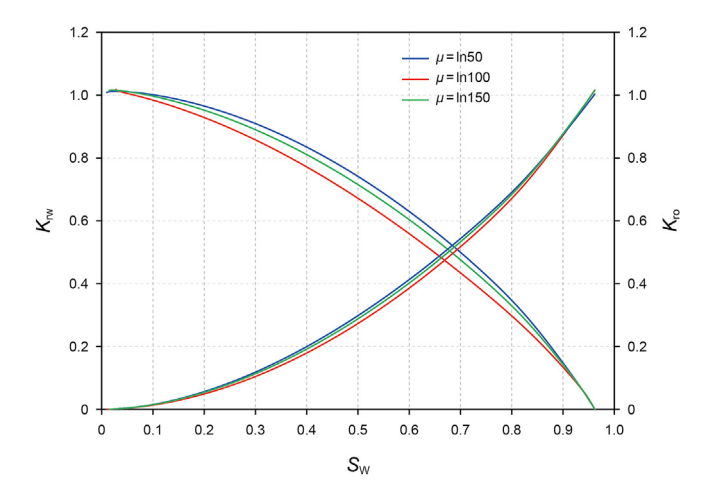


Fig. 10. Relative permeability curves with different PSD of iOM.

be explained as the "lubrication" effect of water and TOC. In iOM pores, when the viscosity of water is lower than that of oil, it acts as a "lubricating film", which enhances the flux of oil. Details explanation can be found in the work of Wang et al. (2019). However, the water phase distributes in the center of pores in OM. A higher oil viscosity will impede the mobility of water. Therefore, as the

viscosity increases, the relative permeability of water phase decreases. This phenomenon is dramatically different from the conclusions of Wang et al. (2019). In their study, the relative permeability of water phase is independent of viscosity ratio in reservoir composed only of iOM. This can be accounted for the Eqs. (S11) and (S12) in Supporting Information, the water flux in adsorbed region and bulk water region is independent of oil viscosity. Although the oil viscosity can affect the apparent viscosity of OWIR. the effect is very limited, as shown in Fig. 9 (b).

## 3.4. Effects of TOC

The TOC is also various in different shale plays. For example, TOC in the lower and upper members of Bakken shale can be as high as 36%, while that of the middle member is less than 1% (Tran et al., 2011). Fig. 13 shows the relationship between TOC and relative permeability, as well as the effective permeability. From Fig. 13(a), We can find that the increase in TOC decreases the effective permeability of both oil and water. This is because the pore size of OM is smaller than that of iOM, which impedes the flow of oil and water. However, the decrease in effective permeability of water phase is smaller than that of oil phase. Based on Fig. 9, the water content of OM is larger than that of iOM, which can make up for the decrease in effective permeability to some extent. In Fig. 13(b), however, the relative permeability of oil and water shows different trends. This is easy to understand, because the smaller pore size in

10

1.0

0.8

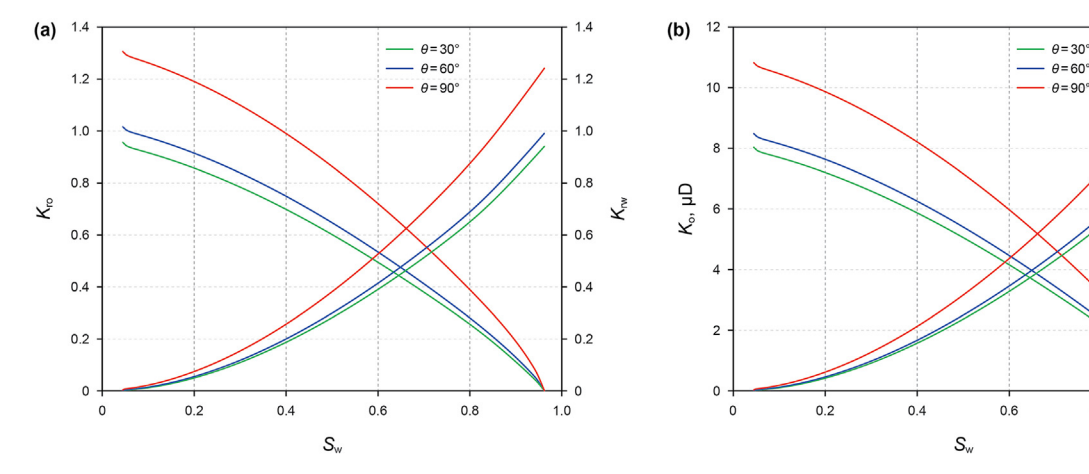


**Fig. 11.** (a) Relative permeability curves with different contact angles; (b) Effective permeability curves with different contact angles. We set  $\theta_w = \theta_0$  in this section.

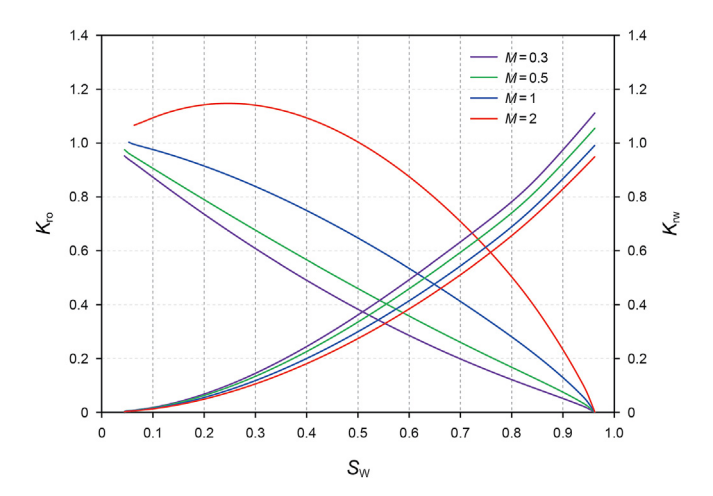


**Fig. 12.** Relative permeability curves with different oil—water viscosity ratios ( $\mu_{\rm wb}=0.8~{\rm mPa}\cdot{\rm s}$ ).

OM also decreases the intrinsic permeability, while the increase in water content only increases the effective permeability of water but decreases the effective permeability of oil. Therefore, based on Eqs. (33) and (34), the relative permeability of water phase increases while that of oil phase decreases.

#### 3.5. Effects of micro-fracture

Fig. 14 and Fig. 15 show the effect of micro-fracture orientation and number on relative permeability and effective permeability. With the increase in  $\beta$ , the orientation of micro-fractures gradually perpendicular to the flow direction (i.e., x direction), the effective permeability of oil and water will decrease as shown in Fig. 14(b). In contrast, the increase in micro-fracture number increases the effective permeability of oil and water as shown in Fig. 15(b), which is due to the larger intrinsic permeability (Eq. (S61)) than nanopores. However, it can be seen from Figs. 14(a) and Fig. 15(a) that the orientation and number of micro-fractures both have minor effects on the relative permeability. This is because these two parameters will affect intrinsic permeability and effective permeability at the same time. According to Eqs. (33) and (34), the influences cancel each other out in the calculation of relative permeability. Therefore, in the calculation of relative permeability, the effect of micro-fractures can be ignored for simplification.

#### 4. Conclusions

In this work, a model for oil—water two-phase flow in single nanopore and micro-fracture of OM and iOM is established by dividing the flow region into adsorbed region, bulk water region, OWIR and bulk oil region. Then we build a discrete spatial

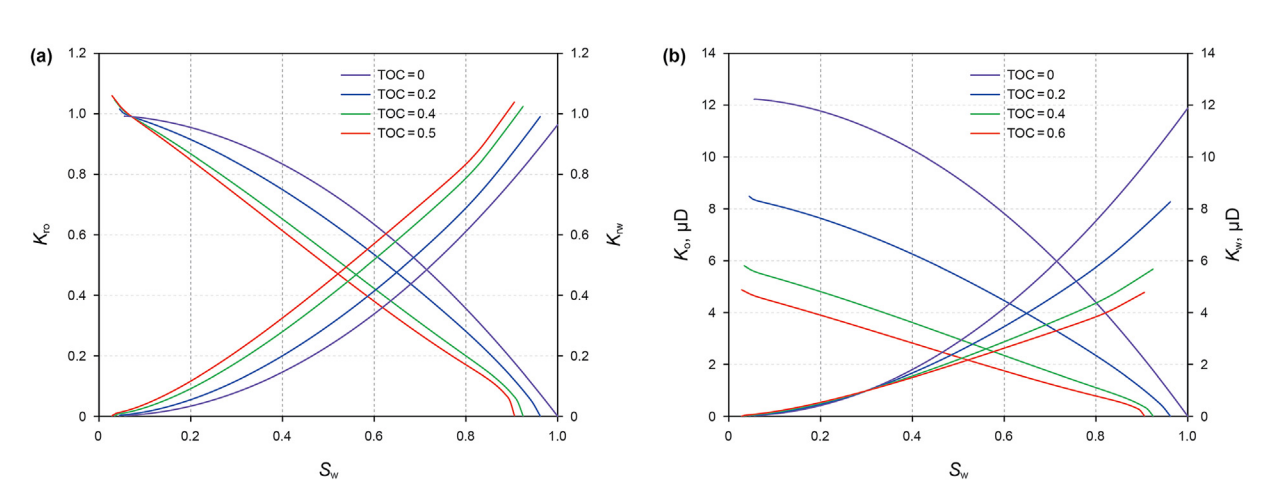


Fig. 13. (a) Relative permeability curves with different TOC values; (b) Effective permeability curves with different TOC values.

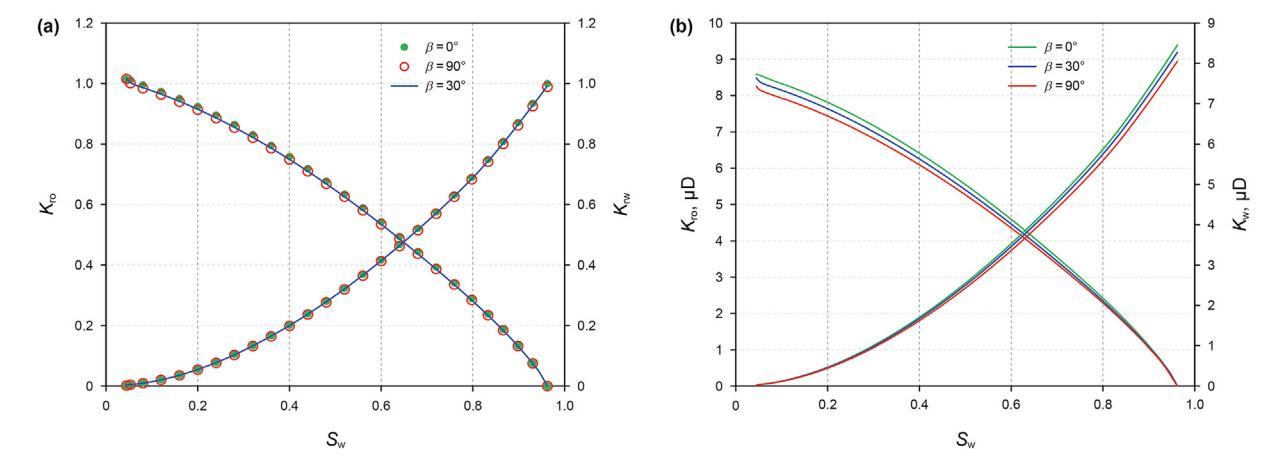
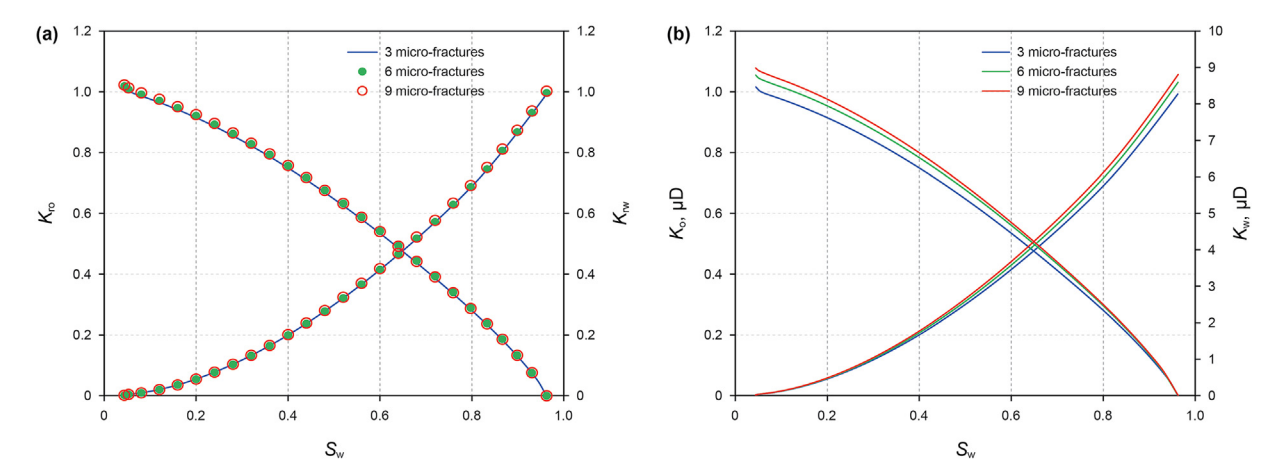


Fig. 14. (a) Relative permeability curves with different micro-fracture orientation; (b) Effective permeability curves with micro-fracture orientation. The micro-fracture number is 3.



**Fig. 15.** (a) Relative permeability curves with different micro-fracture numbers; (b) Effective permeability curves with different micro-fracture numbers.  $\beta = 30^{\circ}$ .

distribution model of OM, iOM and micro-fractures using the QSGS algorithm. The REV-scale relative permeability model is finally established by integrating these two models. The main conclusions are as follows:

- (1) The increase in contact angle in OM and iOM increases the effective permeability and relative permeability of both oil and water. This is because a larger contact angle results in a larger slip length and smaller viscosity of adsorbed regions.
- (2) Different from traditional reservoirs, shale is a dual-wet porous medium. The viscosity ratio of bulk oil to bulk water increases, the relative permeability of water phase increases, while that of oil phase decreases due to the different water—oil distribution between OM and iOM.
- (3) With the increase in TOC, the effective permeability of both oil and water decreases. However, the relative permeability of water increases while that of oil decreases. This is because the OM is hydrophobic, water distributes in the center of pores, resulting in larger water content compared with iOM pores.
- (4) Although the micro-fractures can change the effective permeability of oil and water, they have minor effects on relative permeability. Therefore, the micro-fractures can be ignored when calculating relative permeability.

#### Acknowledgment

This study was supported by the National Natural Science Foundation of China (51804328, 51974348).

## Appendix A. Supplementary data

Supplementary data to this article can be found online at https://doi.org/10.1016/j.petsci.2021.12.024.

# References

- Ba, Y., Liu, H., Li, Q., Kang, Q., Sun, J.J., 2016. Multiple-relaxation-time color-gradient lattice Boltzmann model for simulating two-phase flows with high density ratio. Phys. Rev. E 94, 023310. https://doi.org/10.1103/PhysRevE.94.023310.
- Bui, K., Yucel Akkutlu, I., 2017. Hydrocarbons recovery from model-kerogen nano-
- pores. SPE J. 22, 854–862. https://doi.org/10.2118/185162-PA.
  Cao, G., Lin, M., Jiang, W., Li, H., Yi, Z., Wu, C., 2017. A 3D coupled model of organic matter and inorganic matrix for calculating the permeability of shale. Fuel 204, 129–143. https://doi.org/10.1016/j.fuel.2017.05.052.
- Chen, X., Kianinejad, A., DiCarlo, D.A., 2016. An extended JBN method of determining unsteady-state two-phase relative permeability. Water Resour. Res. 52, 8374–8383. https://doi.org/10.1002/2016WR019204.

- Clarkson, C.R., Solano, N., et al., 2013. Pore structure characterization of North American shale gas reservoirs using USANS/SANS, gas adsorption, and mercury intrusion. Fuel 103, 606–616. https://doi.org/10.1016/j.fuel.2012.06.119.
- Collell, J., Galliero, G., Vermorel, R., Ungerer, P., Yiannourakou, M., Montel, F., Pujol, M., 2015. Transport of multicomponent hydrocarbon mixtures in shale organic matter by molecular simulations. J. Phys. Chem. C 119, 22587–22595. https://doi.org/10.1021/acs.jpcc.5b07242.
- Cui, J., Sang, Q., Li, Y., Yin, C., Li, Y., Dong, M., 2017. Liquid permeability of organic nanopores in shale: calculation and analysis. Fuel 202, 426–434. https:// doi.org/10.1016/i.fuel.2017.04.057.
- Cui, R., Feng, Q., Chen, H., Zhang, W., Wang, S., 2019. Multiscale random pore network modeling of oil-water two-phase slip flow in shale matrix. J. Petrol. Sci. Eng. 175, 46–59. https://doi.org/10.1016/j.petrol.2018.12.026.
- Falk, K., Coasne, B., Pellenq, R., Ulm, F.-J., Bocquet, L., 2015. Subcontinuum mass transport of condensed hydrocarbons in nanoporous media. Nat. Commun. 6, 6949. https://doi.org/10.1038/ncomms7949.
- Fang, C., Sun, S., Qiao, R., 2019. Structure, thermodynamics, and dynamics of thin brine films in oil-brine-rock systems. Langmuir 35, 10341–10353. https:// doi.org/10.1021/acs.langmuir.9b01477.
- Feng, Q., Xu, S., Wang, S., Li, Y., Gao, F., Xu, Y., 2019. Apparent permeability model for shale oil with multiple mechanisms. J. Petrol. Sci. Eng. 175, 814–827. https://doi.org/10.1016/j.petrol.2019.01.038.
- Gupta, S., Koopman, D.C., Westermann-Clark, G.B., Bitsanis, I.A., 1994. Segmental dynamics and relaxation of *n*-octane at solid—liquid interfaces. J. Chem. Phys. 100, 8444—8453. https://doi.org/10.1063/1.466743.
- Honarpour, M., Mahmood, S.M., 1988. Relative-permeability measurements: an overview. J. Petrol. Technol. 40, 963–966. https://doi.org/10.2118/18565-PA.
- Huang, D.M., Sendner, C., Horinek, D., Netz, R.R., Bocquet, L., 2008. Water slippage versus contact angle: a quasiuniversal relationship. Phys. Rev. Lett. 101, 226101. https://doi.org/10.1103/PhysRevLett.101.226101.
- Joseph, S., Aluru, N.R., 2008. Why are carbon nanotubes fast transporters of water? Nano Lett. 8, 452–458. https://doi.org/10.1021/nl072385q.
- Kianinejad, A., Chen, X., DiCarlo, D., 2016. Direct measurement of relative permeability in rocks from unsteady-state saturation profiles. Adv. Water Resour. 94, 1–10. https://doi.org/10.1016/j.advwatres.2016.04.018.
- Koplik, J., Banavar, J.R., 2006. Slip, immiscibility, and boundary conditions at the liquid-liquid interface. Phys. Rev. Lett. 96, 044505. https://doi.org/10.1103/ PhysRevLett.96.044505.
- Li, Z., Jun, Y., Kou, J., 2019. Mixture composition effect on hydrocarbon—water transport in shale organic nanochannels. J. Phys. Chem. Lett. 10, 4291–4296. https://doi.org/10.1021/acs.jpclett.9b01576.
- Lie, K.-A., 2019. An Introduction to Reservoir Simulation Using MATLAB/GNU
  Octave: User Guide for the MATLAB Reservoir Simulation Toolbox (MRST).
  Cambridge University Press.
- Liu, J., Zhao, Y., Yang, Y., Mei, Q., Yang, S., Wang, C., 2020. Multicomponent shale oil flow in real kerogen structures via molecular dynamic simulation. Energies 13, 3815. https://doi.org/10.3390/en13153815.
- Majumder, M., Chopra, N., Andrews, R., Hinds, B.J., 2005. Enhanced flow in carbon nanotubes. Nature 438. https://doi.org/10.1038/438044a, 44-44.
- Mattia, D., Calabrò, F., 2012. Explaining high flow rate of water in carbon nanotubes via solid—liquid molecular interactions. Microfluid. Nanofluidics 13, 125—130. https://doi.org/10.1007/s10404-012-0949-z.
- Nan, Y., Li, W., Jin, Z., 2020. Slip length of methane flow under shale reservoir conditions: effect of pore size and pressure. Fuel 259, 116237. https://doi.org/ 10.1016/j.fuel.2019.116237.
- Naraghi, M.E., Javadpour, F., 2015a. A stochastic permeability model for the shale-gas systems. Int. J. Coal Geol. 140, 111–124. https://doi.org/10.1016/j.coal.2015.02.004.
- Naraghi, M.E., Javadpour, F., 2015b. A stochastic permeability model for the shale-

gas systems. Int. J. Coal Geol. 140, 111–124. https://doi.org/10.1016/j.coal.2015.02.004.

- Naraghi, M.E., Javadpour, F., Ko, L.T., 2018. An object-based shale permeability model: non-Darcy gas flow, sorption, and surface diffusion effects. Transport Porous Media 125, 23—39. https://doi.org/10.1007/s11242-017-0992-z.
- Neuman, S.P., 2008. Multiscale relationships between fracture length, aperture, density and permeability. Geophys. Res. Lett. 35, L22402. https://doi.org/10.1029/2008GL035622.
- Oak, M.J., 1990. Three-phase relative permeability of water-wet Berea. In: SPE/DOE Enhanced Oil Recovery Symposium. https://doi.org/10.2118/20183-MS.
- Perez, F., Devegowda, D., 2020. A molecular dynamics study of soaking during enhanced oil recovery in shale organic pores. SPE J. 25, 832–841. https://doi.org/10.2118/199879-PA.
- Rafatian, N., Capsan, J., 2015. Petrophysical characterization of the pore space in permian wolfcamp rocks. Petrophysics 56. 45–57.
- Singh, H., Cai, J., 2019. A feature-based stochastic permeability of shale: Part 1—validation and two-phase permeability in a utica shale sample. Transport Porous Media 126, 527–560. https://doi.org/10.1007/s11242-018-1073-7.
- Sun, F., Yao, Y., Li, G., Zhang, S., Xu, Z., Shi, Y., Li, X., 2019. A slip-flow model for oil transport in organic nanopores. J. Petrol. Sci. Eng. 172, 139—148. https://doi.org/ 10.1016/j.petrol.2018.09.045.
- Sun, J., Gamboa, E.S., Schechter, D., Rui, Z., 2016. An integrated workflow for characterization and simulation of complex fracture networks utilizing microseismic and horizontal core data. J. Nat. Gas Sci. Eng. 34, 1347–1360. https://doi.org/10.1016/j.jngse.2016.08.024.
- Tahmasebi, P., Javadpour, F., Sahimi, M., 2015. Three-dimensional stochastic characterization of shale SEM images. Transport Porous Media 110, 521–531. https://doi.org/10.1007/s11242-015-0570-1.
- Tran, T., Sinurat, P.D., Wattenbarger, B.A., 2011. Production characteristics of the bakken shale oil. In: SPE Annual Technical Conference and Exhibition. https:// doi.org/10.2118/145684-MS.
- Wang, H., Su, Y., Wang, W., Li, L., Sheng, G., Zhan, S., 2019. Relative permeability model of oil-water flow in nanoporous media considering multi-mechanisms. J. Petrol. Sci. Eng. 183, 106361. https://doi.org/10.1016/j.petrol.2019.106361.
- Wang, M., Wang, J., Pan, N., Chen, S., 2007. Mesoscopic predictions of the effective thermal conductivity for microscale random porous media. Phys. Rev. 75, 036702. https://doi.org/10.1103/PhysRevE.75.036702.
- Wang, S., Javadpour, F., Feng, Q., 2016. Fast mass transport of oil and supercritical carbon dioxide through organic nanopores in shale. Fuel 181, 741–758. https:// doi.org/10.1016/j.fuel.2016.05.057.
- Wang, S., Feng, Q., Javadpour, F., Xia, T., Li, Z., 2015a. Oil adsorption in shale nanopores and its effect on recoverable oil-in-place. Int. J. Coal Geol. 147–148, 9–24.

- https://doi.org/10.1016/j.coal.2015.06.002.
- Wang, W., Su, Y., Sheng, G., Cossio, M., Shang, Y., 2015b. A mathematical model considering complex fractures and fractal flow for pressure transient analysis of fractured horizontal wells in unconventional reservoirs. J. Nat. Gas Sci. Eng. 23, 139–147. https://doi.org/10.1016/j.jngse.2014.12.011.
- Wu, K., Chen, Z., Li, J., Li, X., Xu, J., Dong, X., 2017. Wettability effect on nanoconfined water flow. Proc. Natl. Acad. Sci. Unit. States Am. 114, 3358. https://doi.org/ 10.1073/pnas.1612608114.
- Wu, K., Chen, Z., Li, J., et al., 2019. Nanoconfinement effect on *n*-alkane flow. J. Phys. Chem. C 123, 16456–16461. https://doi.org/10.1021/acs.jpcc.9b03903.
- Yang, Y., Liu, J., Yao, j., et al., 2020. Adsorption behaviors of shale oil in kerogen slit by molecular simulation. Chem. Eng. J. 387, 124054. https://doi.org/10.1016/ i.cei.2020.124054.
- Yiotis, A.C., Psihogios, J., Kainourgiakis, M.E., Papaioannou, A., Stubos, A.K., 2007. A lattice Boltzmann study of viscous coupling effects in immiscible two-phase flow in porous media. Colloids Surf. A Physicochem. Eng. Asp. 300, 35–49. https://doi.org/10.1016/j.colsurfa.2006.12.045.
- Zhan, S., Su, Y., Jin, Z., Wang, W., Li, L., 2020a. Effect of water film on oil flow in quartz nanopores from molecular perspectives. Fuel 262, 116560. https://doi.org/10.1016/j.fuel.2019.116560.
- Zhan, S., Su, Y., Jin, Z., Zhang, M., Wang, W., Hao, Y., Li, L., 2020b. Study of liquid-liquid two-phase flow in hydrophilic nanochannels by molecular simulations and theoretical modeling. Chem. Eng. J. 395, 125053. https://doi.org/10.1016/i.cei.2020.125053.
- Zhang, L., Lu, X., Liu, X., Li, Q., Cheng, Y., Hou, Q., Cai, J., 2019a. Distribution and mobility of crude oil—brine in clay mesopores: insights from molecular dynamics simulations. Langmuir 35, 14818–14832. https://doi.org/10.1021/ acs.langmuir.9b02925.
- Zhang, Q., Su, Y., Wang, W., Lu, M., Sheng, G., 2017a. Apparent permeability for liquid transport in nanopores of shale reservoirs: coupling flow enhancement and near wall flow. Int. J. Heat Mass Tran. 115, 224–234. https://doi.org/10.1016/j.ijheatmasstransfer.2017.08.024.
- Zhang, T., Li, X., Sun, Z., Feng, D., Miao, Y., Li, P., Zhang, Z., 2017b. An analytical model for relative permeability in water-wet nanoporous media. Chem. Eng. Sci. 174, 1–12. https://doi.org/10.1016/j.ces.2017.08.023.
- Zhang, T., Li, X., Yin, Y., He, M., Liu, Q., Huang, L., Shi, J., 2019b. The transport behaviors of oil in nanopores and nanoporous media of shale. Fuel 242, 305–315. https://doi.org/10.1016/i.fuel.2019.01.042.
- Zhang, T., Li, X., et al., 2018. An apparent liquid permeability model of dual-wettability nanoporous media: a case study of shale. Chem. Eng. Sci. 187, 280–291. https://doi.org/10.1016/j.ces.2018.05.016.